

DProST: 6-DoF Object Pose Estimation Using Space Carving and Dynamic Projective Spatial Transformer.

Jaewoo Park¹, Nam Ik Cho¹

¹Department of ECE, INMC, Seoul National University, Seoul, Korea

{bjw0611, nicho}@snu.ac.kr

Abstract

Predicting the pose of an object is a core computer vision task. Most deep learning-based pose estimation methods require CAD data to use 3D intermediate representations or project 2D appearance. However, these methods cannot be used when CAD data for objects of interest are unavailable. Besides, the existing methods did not precisely reflect the perspective distortion to the learning process. In addition, information loss due to self-occlusion has not been studied well. In this regard, we propose a new pose estimation system consisting of a space carving module that reconstructs a reference 3D feature to replace the CAD data. Moreover, Our new transformation module, Dynamic Projective Spatial Transformer (DProST), transforms a reference 3D feature to reflect the pose while considering perspective distortion. Also, we overcome the self-occlusion problem by a new Bidirectional Z-buffering (BiZ-buffer) method, which extracts both the front view and the self-occluded back view of the object. Lastly, we suggest a Perspective Grid Distance Loss (PGDL), enabling stable learning of the pose estimator without CAD data. Experimental results show that our method outperforms the state-of-the-art method on the LINEMOD dataset and comparable performance on LINEMOD-OCCLUSION dataset even compared to the methods that require CAD data in network training. The code will be released soon.

1. Introduction

Object pose estimation aims to estimate the transformation from the object-centered coordinate to the camera-centered one. Since the transformation can be expressed as rotation and translation, each having 3 degrees of freedom, it is also called the 6 DoF pose estimation. Finding the pose is commonly required in AR (augmented reality) [25], robot grasping problems [6, 40, 41, 50], and autonomous driving [5, 46].

Recently, deep learning-based methods have shown out-

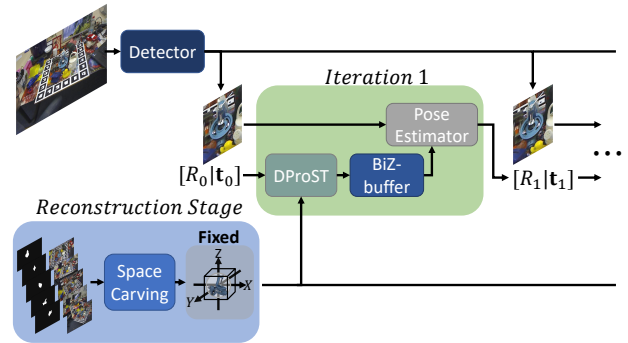


Figure 1. **Overview of our Approach:** We utilize the space carving method to extract the object’s 3D feature from reference images and masks in the reconstruction stage. Based on the object image from the detector, initial pose, and reconstructed 3D, our pose estimation module iteratively refines the object’s pose by predicting the difference between the object image and the pose from the previous step. See the text for details.

standing performance in complex computer vision problems. Therefore, researchers have also proposed methods to apply deep learning to object pose estimation problems, showing excellent performance [23, 33, 39, 45]. Most RGB-based methods predict predefined intermediate features, such as keypoints [28, 32, 38], corners of 3D bounding box [15, 16, 33], or 2D-3D coordinates [3, 9, 24, 30, 42, 43] of the object, which are based on CAD information. On the other hand, render-and-compare-based methods [21, 23] have been proposed to directly estimate the object pose by comparing a rendered image of the object and the input image. These methods also require the CAD of the object to render the object’s appearance. The above methods show excellent performance when accurate 3D data are provided. However, since the shaping of a 3D model of an object is costly, the pose estimation without a CAD model is an essential task to expand the generality of object pose estimation.

Meanwhile, one of the significant problems in pose estimation is that images are taken with a perspective camera that distorts the scene depending on the distance. Al-

though the camera’s intrinsic parameters are usually available, previous methods used these parameters (1) after the output of the neural network by applying the PnP-algorithm [9, 24, 30, 42, 43, 48], or (2) before going into the neural network on the rendering tool [21, 23]. Since both processes are generally non-differentiable, they fail to reflect the perspective distortion process to the network or the objective function. Also, very little research considered self-occlusion, although it is one of the main causes of 3D information loss. To the best of our knowledge, only SO-Pose [9] has proposed a method to deal with the self-occlusion issue, but it is a method that requires 3D models for the intermediate representations.

Therefore, we propose a method that reflects the perspective distortion in the training phase without requiring CAD models. Our method proceeds in two stages. The first is the reconstruction stage, where we generate 3D features from reference images and masks. The second is the pose estimation stage that iteratively refines the pose of the detected object. The reconstruction stage is inspired by studies such as [29] and [37]. But unlike existing methods, we use a simple space-carving-based reconstruction module [20] without using a neural network or a depth map.

Each iteration of our pose estimation stage consists of three sub-steps, which are Dynamic Projective Spatial Transformer (DProST), Bidirectional Z-buffer (BiZ-buffer), and the convolutional neural network (CNN) based Pose Estimator. DProST transforms the reconstructed 3D feature into the 3D feature of the pose from the previous step. Also, it aligns the features along the ray to reflect perspective distortion. DProST is inspired from the ProST in [10]. However, unlike the target of [10] where the distance between the camera and the object is fixed, the distance changes in the 6DoF problem, requiring an exponentially large size of grid. We overcome this issue by letting the grid move dynamically and focusing only on the target Region of Interest (RoI). The second sub-step is the BiZ-buffer, which extracts both visible and self-occluded 2D features from the output of DProST to inform the object’s current pose to the Pose Estimator. Thanks to DProST, which aligns the 3D feature considering perspective distortion, the BiZ-buffer method can extract 2D features via a simple index pooling. Then, the Pose Estimator compares the 2D features and the object image from the detector to predict the pose difference. Figure 1 shows the overview of our method. In addition, to teach the Pose Estimator without CAD information, we propose a new objective function, Perspective Grid Distance Loss (PGDL). Since our new loss function does not use CAD data, it is free from the object shape bias.

Our contributions are summarized as follows:

- We propose a novel CAD-less 6D object pose estimation system based on space-carving that extracts 3D feature from reference images and masks.

- We propose **Dynamic Projective Spatial Transformer (DProST)** that efficiently transforms 3D features to an estimated pose considering perspective distortion.
- We propose **Bidirectional Z-buffering (BiZ-buffer)** method that extracts the the object’s visible and self-occluded parts from the 3D feature.
- We propose **Perspective Grid Distance Loss (PGDL)**, which can train the pose estimator in a CAD-less environment and is free from object shape bias.
- We confirm that our CAD-less method shows better or comparable performance to CAD-based methods on LINEMOD and LINEMOD-OCCLUSION benchmarks.

2. Related Work

2.1. RGB-based Pose Estimation

Deep learning-based RGB pose estimation methods can be divided into two types. The first is to estimate the 3D intermediate representation and then find the matching transform with the PnP-algorithm [22]. For example, [16, 33] used 3D bounding box estimation, [32, 38] detected keypoints of an object, and [24, 30, 42, 48] predicted 2D-3D coordinates to estimate the pose of the object. [9] raised the problem of self-occlusion and suggested a method to consider occluded coordinates in learning. However, these methods, which estimate an intermediate representation of the 3D model, have limitations in that they learn the position of the visible part for each object, not the geometrical rule of the translation and rotation itself in 3D.

The second type is a render-and-compare-based approach that estimates the pose by comparing the rendered image of the 3D model and the object image. For example, [17] extracted features from object images using a neural network and optimized the pose directly by backpropagation, and [47] proposed rendered silhouette comparing based pose matching method. On the other hand, [23] used the object rendered in initial pose and the object image to refine the pose difference iteratively. Also, in this method, the performance of regression-based pose estimation was greatly improved by the disentangled representation of rotation and translation. Based on an iterative fashion similar to [23], the single view method in [21] showed the most superior performance in the object pose estimation challenge [14] by using a large number of synthetic images for training. [21, 23] did not require a 3D intermediate representation like other pose estimation methods. Also, they can be used for general objects because they learn the three-dimensional relation between input-rendering rather than estimating the object’s shape. However, since both methods use an external renderer which is non-differentiable, their networks

have limitations in learning the perspective distortion of the objects, and they need a 3D model.

2.2. 3D Feature Reconstruction and Projection

Although most RGB-based pose estimation methods require 3D models, using the 3D model can be problematic because the generation cost is high. Accordingly, methods using a module that reconstruct the shape of an object have been proposed instead of using a 3D model. In the 3D reconstruction problem, one of the widely used methods is space carving [20], which projects rays passing through each pixel of multiple views of an object into a 3D volume and extracts the overlapping part. Methods based on deep learning have also been recently proposed, such as the voxel expression methods [7,27,37], mesh expression methods [11,44], and implicit 3D learning [1,26]. Based on these reconstruction methods, [29] learned a neural network that reconstructs 3D latent features of the object using multi-view reference images and masks, then optimized the pose to reduce depth error. This method can be used for general objects, but it requires a depth map and various types of 3D models for training.

On the other hand, methods for projecting 3D features into 2D, considering perspective distortion, have also been proposed in [10,37]. In particular, [10] proposed ProST, which used the grid of the existing spatial transformer with consideration of perspective projection, and precisely registered 3D CT to X-ray. The target of [10] was only estimating the rotation, so the distance to the camera was set, and the RoI of the cone-beam grid was limited. However, the RoI space is too wide to apply ProST to 6DoF pose estimation that also considers translation. If we use a dense grid, too much memory and computation are required, and if we widen the interval in the grid, the quality of the projection image deteriorates.

Considering the pros and cons of the above-referenced methods, we propose a new pose estimation algorithm that does not require CAD. The overall configuration is based on a framework that iteratively predicts the pose difference of an object with a neural network. We use the space carving method to reconstruct the 3D feature from reference images and masks. Also, to increase the efficiency of [10], we propose a new DProST that can be used for 6 DoF. In addition, we propose a new projection method named BiZ-buffering that tackles the self-occlusion problem. Lastly, we propose a new loss (PGDL) based on a grid extracted with DProST, which elaborately considers the perspective distortion of the object in the image.

3. Method

3.1. Framework Overview

Our proposed method is designed to work in an iterative render-and-compare fashion inspired by [21,23]. However, instead of the rendered image projected from CAD, our method reconstructs the 3D feature from reference images and use it to obtain the object’s projected appearance. We first reconstruct $\mathcal{F}^{ref} \in \mathbb{R}^{S \times S \times S \times 3}$ which is the 3D feature of an object from N reference images ($\{X_n^{ref} | n \in (1, \dots, N)\}$) and corresponding masks ($\{M_n^{ref} | n \in (1, \dots, N)\}$), sampled from the training set, where S is the number of voxels along each axis. Note that for each object, \mathcal{F}^{ref} is fixed during training and testing.

In pose estimation stage, using a detector such as [36], we first find the bounding box $(\hat{x}^B, \hat{y}^B, \hat{w}^B, \hat{h}^B)$ of the object to crop the object image X^B . Then for each iteration step t , by using the DProST module, we transform \mathcal{F}^{ref} to $\hat{\mathcal{F}}_{t-1}^T \in \mathbb{R}^{\hat{h}^B \times \hat{w}^B \times N_z \times 3}$ with the pose estimation from the previous step $\hat{T}_{t-1} = [\hat{R}_{t-1} | \hat{\mathbf{t}}_{t-1}] \in \mathbb{R}^{3 \times 4}$, where \hat{R}_{t-1} and $\hat{\mathbf{t}}_{t-1}$ are the rotation matrix and the translation vector predicted from the previous step $t - 1$ respectively, and N_z is the number of points in the grid along the ray. Then we use BiZ-buffering to project $\hat{\mathcal{F}}_{t-1}^T$ into two 2D features, one is a front view $\hat{F}_{t-1}^f \in \mathbb{R}^{\hat{h}^B \times \hat{w}^B \times 3}$ of the object visible from the camera, and the other is a back view $\hat{F}_{t-1}^b \in \mathbb{R}^{\hat{h}^B \times \hat{w}^B \times 3}$ which is the self-occluded part. Finally, by comparing \hat{F}_{t-1}^f and \hat{F}_{t-1}^b with X^B , our pose estimator refines the given pose to the $\hat{T}_t = [\hat{R}_t | \hat{\mathbf{t}}_t]$. In the following subsections, we describe the details of 3D feature reconstruction and pose estimation based on space carving, DProST, BiZ-buffering, and the loss term PGDL.

3.2. 3D Feature Reconstruction

We aim to generate the object’s 3D feature \mathcal{F}^{ref} from the reference images ($\{X_n^{ref} | n \in (1, \dots, N)\}$) and corresponding masks ($\{M_n^{ref} | n \in (1, \dots, N)\}$), which are sampled from the training set. As in [29], we normalize the radius of the 3D object to one. Then, to cover the object, we generate a 3D canvas as a voxel grid $\mathcal{A}^{ref} \in \mathbb{R}^{S \times S \times S \times 3}$ in $-1 \leq (X, Y, Z) \leq 1$, which is divided uniformly to S^3 voxels, and each contains the coordinates of itself. Then for each reference index $n \in (1, \dots, N)$, \mathcal{A}^{ref} is projected with the given camera intrinsic parameter $K \in \mathbb{R}^{3 \times 3}$ and the pose of the n -th reference $T_n^{ref} = [R_n^{ref} | \mathbf{t}_n^{ref}]$ to find the region in the image where the canvas grid is projected. Note that for the simplicity of notation, transforming coordinates according to any matrix (or pose) T^* will be written as $T^*(\cdot)$ in the rest of the paper. Hence, we assign the pro-

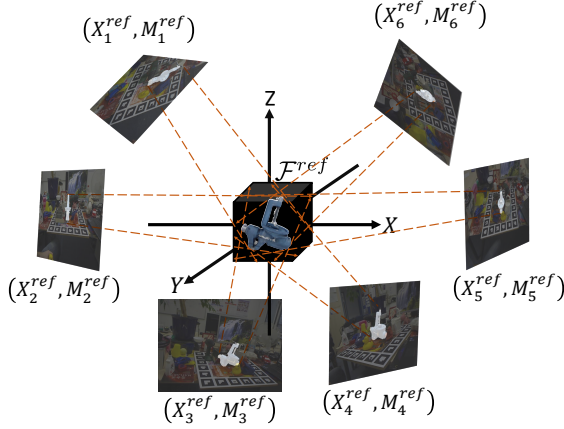


Figure 2. **3D Feature Reconstruction:** We visualize the object shaping and coloring process of generating \mathcal{F}^{ref} . Only the voxels projected into every object area of $M_{n \in (1, \dots, N)}^{ref}$ remain positive, and others are cut off. Also, the values of valid \mathcal{F}^{ref} are the average of the projected pixels over $X_{n \in (1, \dots, N)}^{ref}$.

jected grid location in $\mathcal{G}_n^{ref} \in \mathbb{R}^{S \times S \times S \times 2}$ as

$$\mathcal{G}_n^{ref} \simeq K (T_n^{ref} (A^{ref})) \quad (1)$$

where \simeq is means the projection of homogeneous coordinates. Then, by using \mathcal{G}_n^{ref} as grid, we apply grid sampling method proposed in [18] to generate a 3D RGB feature $\mathcal{X}_n^{ref} \in \mathbb{R}^{S \times S \times S \times 3}$ from X_n^{ref} and 3D mask feature $\mathcal{M}_n^{ref} \in \mathbb{R}^{S \times S \times S \times 1}$ from M_n^{ref} by

$$\mathcal{X}_n^{ref} = X_n^{ref} \left((g_n^{ref})_x, (g_n^{ref})_y \right) \quad (2)$$

$$\mathcal{M}_n^{ref} = \begin{cases} 1 & \text{if } M_n^{ref} \left((g_n^{ref})_x, (g_n^{ref})_y \right) = 1 \\ 0 & \text{otherwise} \end{cases} \quad (3)$$

where $(g_n^{ref})_x$ and $(g_n^{ref})_y$ are (x, y) coordinates in \mathcal{G}_n^{ref} . Note that we use nearest neighbor interpolation to extract values from non-integer locations.

We average the $\mathcal{X}_{n \in (1, \dots, N)}^{ref}$'s over references to obtain the integrated 3D RGB feature \mathcal{X}^{ref} , and multiply $\mathcal{M}_{n \in (1, \dots, N)}^{ref}$'s over references to get the shape-carved 3D mask feature \mathcal{M}^{ref} . In the end, the 3D feature of the object is calculated by

$$\mathcal{F}^{ref} = \mathcal{X}^{ref} \odot \mathcal{M}^{ref} \quad (4)$$

where \mathcal{F}^{ref} is an RGB 3D feature with carved shape which has the object information in voxel fashion, and \odot is an elementwise multiplication. Concept of carving process is visualized in Figure 2.

In addition, since \mathcal{F}^{ref} is generated with finer detail when the object area in the reference image is wide while the rotation of the reference images is evenly distributed, we set the first reference image as the sample with the largest

object mask in the training set. Then, based on the geodesic distance of the rotation matrix, we use the farthest point sampling (FPS) algorithm to select the other reference images.

3.3. Object Pose Estimation

3.3.1 Dynamic Projective Spatial Transformer

Concept and Role of DProST Module. We will briefly explain the concept of our DProST in this subsection and explain its details in the following subsections. First, a default grid and coefficient, which model ray from camera to image plane, are generated as shown in Figure 3(a). Then for each pose estimation, the RoI region of the default grid is cropped and pushed along the ray from the camera to 3D space as in Figure 3(b), (c). Here, the coefficient indicates the direction of movement for each grid point. Finally, the grid is transformed by the given pose to cover F^{ref} as in Figure 3(d), which is then used for grid sampling on F^{ref} . The transformed grid covers F^{ref} if the object is accurately detected because of the following three facts. First, the projection of the object is included in the bounding box of the image. Second, the size of the translation vector is the distance from the origin to the camera. Third, F^{ref} is in the unit sphere on the origin, which can be covered by a grid with thickness two.

DProST has two roles in our framework. The first role is a part of renderer since the DProST extracts 3D features from F^{ref} according to the given pose. The second role is a loss calculation module. Since the whole process of DProST is differentiable, it can be used as a path for gradient flow from the image space to the pose space, which can be used to teach the pose estimator.

Default Grid Generation. Given the focal length f of the camera, principal points (p_x, p_y) , and the image size (H, W) , we fix the camera's location on the origin and the direction to $+Z$, and find the 3D coordinates of each pixel on the 3D image plane \mathcal{I} , where $\mathcal{I}_X \in [p_x - W, p_x]$, $\mathcal{I}_Y \in [p_y - H, p_y]$, and $\mathcal{I}_Z = f$. Hence, the 3D coordinates of the pixels (i, j) on the image plane can be written as $\mathcal{I}(i, j) = (p_x - i, p_y - j, f)$. Then, we create the default grid $\mathcal{G} \in \mathbb{R}^{H \times W \times N_z \times 3}$, where each grid column $\{\mathcal{G}(i, j, \cdot) \in \mathbb{R}^{N_z \times 3} | 1 \leq i \leq W, 1 \leq j \leq H\}$ in \mathcal{G} is on the line which penetrates the origin O and each $\mathcal{I}(i, j)$, and the grid values in the $\mathcal{G}(i, j, \cdot)$'s have uniform intervals. We also create the coefficient $\mathcal{C} \in \mathbb{R}^{H \times W \times N_z \times 3}$, which contains the normal vector from each point in \mathcal{G} to corresponding projected 3D images pixels. Since our grid can be dynamically pushed through the rays in the following DProST steps, the range of \mathcal{G} and \mathcal{C} can be restricted in the unit sphere. Thus,

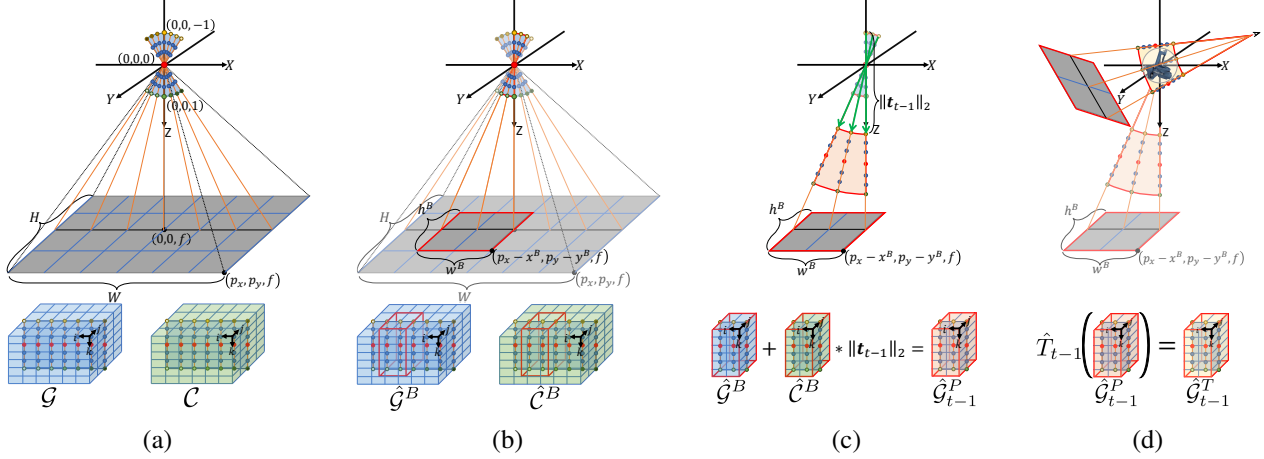


Figure 3. **Dynamic Projective Spatial Transformer**: We visualize the concept of grid moving in the first row and actual tensor calculation in the second row. (a) shows the default grid \mathcal{G} and coefficient \mathcal{C} which are based on the given camera parameters and image size. We visualize the 3D image plane in gray, each 3D pixel as a cross of sky blue line, rays passing through the origin and each 3D pixel as orange lines, the grid as colored vertices. Note that we express the brightness of the grid vertices differently for each ray. (b) illustrates the grid cropping process to extract $\hat{\mathcal{G}}^B$ and $\hat{\mathcal{C}}^B$ which are indicated in red boxes. (c) shows the grid pushing process based on $\|\hat{\mathbf{t}}_{t-1}\|_2$, $\hat{\mathcal{G}}^B$, and $\hat{\mathcal{C}}^B$ to extract the pushed grid $\hat{\mathcal{G}}_{t-1}^P$. We notate the broadcasting multiplication of scalar on tensor as $*$. Lastly, (d) shows the grid transformation process, which transforms $\hat{\mathcal{G}}_{t-1}^P$ into $\hat{\mathcal{G}}_{t-1}^T$ with \hat{T}_{t-1} .

$\mathcal{G}(i, j, k)$ and the $\mathcal{C}(i, j, k)$ can be written as:

$$\mathcal{G}(i, j, k) = \frac{\mathcal{I}(i, j)}{\|\mathcal{I}(i, j)\|_2} \left(\frac{2}{N_z}(k-1) - 1 \right) \quad (5)$$

$$\mathcal{C}(i, j, k) = \frac{\mathcal{I}(i, j)}{\|\mathcal{I}(i, j)\|_2} \quad (6)$$

where $k \in (1, \dots, N_z)$ is an index of points in the ray path following the direction from the origin to a 3D image pixel $\mathcal{I}(i, j)$, and N_z is the size of the grid on each ray. Since f and (H, W) are usually fixed constants, \mathcal{G} and \mathcal{C} are made only once when starting the training phase. See Figure 3(a) for a visual explanation.

Grid Cropping, Pushing, and Transformation. For each pose estimation, we extract the grid and the coefficient in a detected bounding box to focus on the RoI and reduce the number of points in the grid. As shown in Figure 3(b), a cropped grid $\hat{\mathcal{G}}^B \in \mathbb{R}^{\hat{h}^B \times \hat{w}^B \times N_z \times 3}$ and coefficient $\hat{\mathcal{C}}^B \in \mathbb{R}^{\hat{h}^B \times \hat{w}^B \times N_z \times 3}$ can be written as

$$\hat{\mathcal{G}}^B = \{\mathcal{G}(i, j, k) \mid (i, j) \in S^B\} \quad (7)$$

$$\hat{\mathcal{C}}^B = \{\mathcal{C}(i, j, k) \mid (i, j) \in S^B\} \quad (8)$$

where $\hat{\mathcal{G}}^B$ and $\hat{\mathcal{C}}^B$ are the grid and coefficient of rays projected in the object bounding box and S^B is $\{(i, j) \mid i \in [p_x - \hat{x}^B, p_x - (\hat{x}^B + \hat{w}^B)], j \in [p_y - \hat{y}^B, p_y - (\hat{y}^B + \hat{h}^B)]\}$, which is the set of pixels in bounding box of 3D image plane.

After the cropping, since the distance from the object to the camera is the size of the translation vector, we push $\hat{\mathcal{G}}^B$ along each ray by $\|\hat{\mathbf{t}}_{t-1}\|_2$ and transform with \hat{T}_{t-1} to

cover the object in the unit sphere as shown in Figures 3(c) and (d). Since the distance to both ends of the grid point on a ray is set to two in the default grid \mathcal{G} , the transformed grid $\hat{\mathcal{G}}_{t-1}^T$ is in the form of a part of the shell of a sphere with the thickness of two. The transformed grid tightly wraps around the 3D object as in Figure 3(d) when the bounding box is accurate because the size of the \mathcal{F}^{ref} is normalized to a unit sphere. Since $\hat{\mathcal{C}}^B$ is the normal vector of grid to image space direction, the pushed grid $\hat{\mathcal{G}}_{t-1}^P$ and transformed grid $\hat{\mathcal{G}}_{t-1}^T$ can be written as

$$\hat{\mathcal{G}}_{t-1}^P = \hat{\mathcal{G}}^B + \|\hat{\mathbf{t}}_{t-1}\|_2 \hat{\mathcal{C}}^B \quad (9)$$

$$\hat{\mathcal{G}}_{t-1}^T = \hat{T}_{t-1} \left(\hat{\mathcal{G}}_{t-1}^P \right). \quad (10)$$

Thanks to the pushing process, DProST does not need to generate the grid \mathcal{G} outside the unit sphere, which reduces the amount of grid and computation exponentially. Also, by focusing the dense grid only in the RoI space, the projection quality in the following BiZ-buffering is dramatically improved. After the pushing process, we apply rigid transformation \hat{T}_{t-1} to $\hat{\mathcal{G}}_{t-1}^P$ to cover the reference object feature \mathcal{F}^{ref} . Finally, we apply the trilinear interpolation-based grid sampling method, which is a 3D version of bilinear interpolation used in [10, 18], to \mathcal{F}^{ref} with grid $\hat{\mathcal{G}}_{t-1}^T$ to extract the 3D feature $\hat{\mathcal{F}}_{t-1}^T$ that reflects perspective distortion and the pose \hat{T}_{t-1} . An additional explanation about grid sampling is provided in the supplementary material.

3.3.2 Bidirectional Z-buffering

To compare the estimated pose and the image of the object, we extract two 2D features from $\hat{\mathcal{F}}_{t-1}^T$. By denoting the third dimension of $\hat{\mathcal{F}}_{t-1}^T$, which has N_z points along the k -axis as in a tensor form of Figure 3, the front view feature ($\hat{F}_{t-1}^f \in \mathbb{R}^{\hat{h}^B \times \hat{w}^B \times 3}$) from $\hat{\mathcal{F}}_{t-1}^T$ in the $-k$ direction is obtained by choosing the closest point to the camera on each ray. The back view feature ($\hat{F}_{t-1}^b \in \mathbb{R}^{\hat{h}^B \times \hat{w}^B \times 3}$) in the $+k$ direction is obtained by choosing the farthest points to cover the self-occluded surface region of the object. Thanks to the DProST method, which aligns grid along the ray, a simple index pooling along the k -axis can extract both \hat{F}_{t-1}^f and \hat{F}_{t-1}^b as

$$\hat{F}_{t-1}^f(i, j) = \hat{\mathcal{F}}_{t-1}^T \left(i, j, \min\{k_Z(i, j)\} \right) \quad (11)$$

$$\hat{F}_{t-1}^b(i, j) = \hat{\mathcal{F}}_{t-1}^T \left(i, j, \max\{k_Z(i, j)\} \right) \quad (12)$$

where $k_Z(i, j) = \{k | \hat{\mathcal{F}}_{t-1}^T(i, j, k) \neq \mathbf{o}\}$ and the \mathbf{o} is the three dimensional zero vector to be compared with RGB values to find valid voxels.

3.3.3 Perspective Grid Distance Loss

We then use a CNN to compare the object image X^B from the detector with the extracted features (\hat{F}_{t-1}^f and \hat{F}_{t-1}^b) from BiZ-buffering. We estimate the pose difference $\Delta \hat{T}_t = [\Delta \hat{R}_t | \Delta \hat{\mathbf{t}}_t]$ of object image and front view from BiZ-buffer, which is then applied to $\hat{T}_{t-1} = [\hat{R}_{t-1} | \hat{\mathbf{t}}_{t-1}]$ to output the refined pose $\hat{T}_t = [\hat{R}_t | \hat{\mathbf{t}}_t]$. We follow the disentangled representation of rotation and translation proposed in [21], which shows great performance in regression-based pose estimation. However, unlike [21], since we assume the absence of CAD in our method, the Point Matching (PM) loss [21, 23, 45], which requires the vertices of CAD, cannot be used. To solve this problem, we replace the PM loss to Perspective Grid Distance Loss (PGDL), which is the distance between the ground truth grid $\bar{\mathcal{G}}^T$ based on the label pose $\bar{T} = [\bar{R} | \bar{\mathbf{t}}]$ and the predicted grid $\hat{\mathcal{G}}_t^T$ based on the estimated pose $\hat{T}_t = [\hat{R}_t | \hat{\mathbf{t}}_t]$. Specifically, the loss is formulated as

$$\begin{aligned} \mathcal{L}_t^{PGDL} & \left(T, \hat{T}_t \right) \\ & = \frac{1}{|\hat{\mathcal{G}}^B|} \sum_{(i, j, k) \in S^G} \left\| \bar{\mathcal{G}}^T(i, j, k) - \hat{\mathcal{G}}_t^T(i, j, k) \right\|_2 \end{aligned} \quad (13)$$

where $S^G = \{(i, j, k) | 1 \leq i \leq \hat{h}^B, 1 \leq j \leq \hat{w}^B, 1 \leq k \leq N_z\}$ and $|\hat{\mathcal{G}}^B|$ is the number of the grid in $\hat{\mathcal{G}}^B$. More details about PGDL formulation are given in the supplementary material.

Also, in order to help the pose estimator to find the distance to the object, which is the grid pushing distance, we use an additional loss term named Pushing Distance Loss as

$$\mathcal{L}_t^{PDL} \left(\|\bar{\mathbf{t}}\|_2, \|\hat{\mathbf{t}}_t\|_2 \right) = \left| \|\bar{\mathbf{t}}\|_2 - \|\hat{\mathbf{t}}_t\|_2 \right|_1 \quad (14)$$

which is the $L1$ distance between the size of the predicted translation vector $\hat{\mathbf{t}}_t$ and the size of the ground truth translation vector $\bar{\mathbf{t}}$.

Finally, the overall loss to train our network on each iteration t is the combination of above two losses,

$$\mathcal{L}_t^{total} = \mathcal{L}_t^{PGDL} + \lambda^{PDL} \mathcal{L}_t^{PDL} \quad (15)$$

where λ^{PDL} is the balance factor for \mathcal{L}_t^{PDL} .

In order to calculate \mathcal{L}_t^{total} from the current predictions of the pose estimator, the output of DProST in the following iteration ($t+1$) is used. Hence, for the last iteration, DProST is applied once again for loss calculation. However, unlike other render-and-compare-based methods [21, 23], which require transformation twice per iteration for each rendering and loss calculation in the training phase, our method unifies both transformations in DProST, which increases the computation efficiency and reduces memory.

Besides the fact that no CAD model is required, the PGDL has some advantages compared to commonly used PM loss [21, 23, 45]. First, since the loss function is based on the distance of uniformly distributed grids rather than 3D vertices in each object's CAD model, the PGDL is relatively free from object shape biases. Second, since the projective grid used in PGDL reflects the perspective distortion by considering the ray path, the PGDL elaborately synchronizes with object appearance in the image space. For example, even if the PM distance is identical in the 3D space, the PGDL outputs a larger value when a part of the object close to the camera is misaligned, since it causes larger displacement in image space. Thanks to the above advantages, the PGDL-based model shows superior performance than the PM loss on the benchmark dataset.

4. Experiments

4.1. Datasets and Evaluation Metrics

The performance is tested on LINEMOD (LM) [13] and LINEMOD-OCCLUSION (LMO) [2] dataset. The LM consists of 13 objects with around 1.2K images per object. We follow the settings in [3], which uses 15% of the data for the training and the others for the test. The LMO dataset is a subset of the LM dataset consisted of 8 objects in more cluttered scenes. We also use the official pbr dataset from the BOP challenge [14] in training with a real image training set and do not use any additional synthetic image dataset.

We employ the ADD score [13], which measures the mean distance of vertices between two transformed 3D



Figure 4. **Qualitative Results on the LINEMOD.** For each category, the first row shows a detected object image. The second row is the projected front view of the 3D feature, which is reconstructed in our 3D feature extractor, projected by DProST and BiZ-buffered with the predicted pose. The last row shows the object images with ground truth pose contour in green and predicted pose contour in blue.

Method	[45]	[23]	[29]	[38]	[42]	[17]	[9]	Ours
ape	-	77.0	83.7	77.6	-	79.5	-	91.4
benchwise	-	97.5	91.3	99.6	-	100.0	-	100.0
cam	-	93.5	74.3	95.9	-	99.2	-	98.3
can	-	96.5	83.4	93.6	-	99.8	-	99.4
cat	-	82.1	84.4	93.5	-	97.9	-	97.1
driller	-	95.0	90.6	97.2	-	99.0	-	99.8
duck	-	77.7	71.3	87.0	-	80.3	-	86.9
eggbox*	-	97.1	39.3	99.6	-	100.0	-	95.6
Glue*	-	99.4	94.7	98.7	-	98.3	-	100.0
holepuncher	-	52.8	53.7	92.5	-	96.9	-	95.9
iron	-	98.3	70.0	98.1	-	100.0	-	99.5
lamp	-	97.5	87.8	96.9	-	99.8	-	99.7
phone	-	87.7	90.3	98.3	-	98.9	-	94.5
Average	62.7	88.6	78.1	94.5	93.7	96.1	96.0	96.8

Table 1. **Results on LM.** The comparison of other baseline methods and our method in terms of ADD(-S) score. Objects annotated with (*) indicates symmetric pose ambiguity.

models using the ground truth pose and the estimated pose. The pose is considered correct if the mean distance is less than 10% of object diameter. Note that we do not need the 3D data but use them only for measuring the ADD score for a fair comparison. We also use the ADD-S metric [13] for the symmetric objects, which measures the deviation to the closest point from each predicted and ground-truth model.

4.2. Experiment Setup

Implementation Details. Our pipeline is implemented based on Pytorch [31] and Pytorch3d [34] framework. The experiments are conducted on an Intel Core i7-7700K CPU with an NVIDIA TITAN Xp GPU. We use ADAM optimizer [19] with a learning rate of 0.0001 until the 2,000 epochs, then divided by ten and trained 1,000 epochs more.

In the reconstruction stage, we use 8 reference images ($N = 8$) to generate reference features for each object and use the number of voxels along the axis as 128 ($S = 128$) based on the experimental results of [29]. In the DProST module, 100 grid points ($N_z = 100$) per ray is used. Since N_z controls the density of the grid along the z-axis, the projection results are clearer with large N_z . But, it has a trade-

Method	[45]	[23]	[48]	[38]	[42]	[17]	[9]	Ours
ape	9.6	59.2	-	20.9	46.8	31.1	48.4	49.4
can	45.2	63.5	-	75.3	90.8	80.0	85.8	76.8
cat	0.9	26.2	-	24.9	40.5	25.6	32.7	32.5
driller	41.4	55.6	-	70.2	82.6	73.1	77.4	81.6
duck	19.6	52.4	-	27.9	46.9	43.0	48.9	46.5
eggbox*	22.0	63.0	-	52.4	54.2	51.7	52.4	34.2
glue*	38.5	71.7	-	53.8	75.8	54.3	78.3	69.6
holepuncher	22.1	52.5	-	54.2	60.1	53.6	75.3	52.7
Average	24.9	55.5	47.3	47.5	62.2	51.6	62.4	55.4

Table 2. **Results on LMO.** The accuracies of baseline methods and our method in terms of ADD(-S) score. Objects annotated with (*) indicate symmetric pose ambiguity.

off that the amount of computation increase linearly with N_z . Also, since the size of the reference feature is fixed, the quality of projection is saturated when N_z is larger than 100. We use λ^{PDL} as 1 in Equation (15) since the scale of both loss terms are similar. Details about experiments on hyper parameters are given in the supplementary material.

We use a pretrained ResNet34 [12] on ImageNet [8] as a pose estimator and change the number of units in the first and the last layer to take projected front/back views and object image, and output the disentangled representation as in [21]. Here, two vectors are predicted to recover the relative rotation matrix [49]. Also, pixel-level movement and scaling ratio are predicted to recover the relative translation vector. To prevent the object from being out of sight in the initial pose, we set the initial translation vector to fit the projection of the 3D reference feature into the bounding box with identity matrix as the initial pose’s rotation. Refer to [21, 23] for details of the disentangled output representation and initial pose formulation. Also, we use distinct weights for the pose estimator in each step to teach the models to work in a cascade fashion [4] that shows better performance than that of iterative models.

Object Zoom-In. Since small object images can be problematic for the recognition of translation along the z-axis of a camera, we zoom in the detected object as [21, 23, 24, 42]

Iteration	1	2	3	3	3
BiZ-buffer	✓	✓		✓	✓
Loss	PGDL	PGDL	PGDL	PM	PGDL
ape	80.5	90.9	89.6	71.8	91.4
benchwise	91.8	100.0	96.1	100.0	100.0
cam	80.7	98.6	95.9	95.2	98.3
can	83.9	99.4	98.4	95.0	99.4
cat	87.0	97.2	97.9	86.5	97.1
driller	92.2	99.0	99.8	98.3	99.8
duck	47.5	86.9	89.5	85.6	86.9
eggbox*	99.6	95.7	99.9	100.0	95.6
Glue*	99.3	99.9	99.6	99.7	100.0
holepuncher	91.5	95.8	97.1	92.2	95.9
iron	96.3	99.5	99.5	99.6	99.5
lamp	97.8	99.8	99.9	100.0	99.7
phone	82.0	91.6	94.1	91.2	94.5
Average	86.9	96.5	96.7	93.5	96.8

Table 3. **Ablation Study Results on LM.** We compare the effectiveness of the number of iterations, BiZ-buffer, and PGDL on LM dataset.

to a fixed size 128×128 while keeping the aspect ratio of the image. Specifically, to train our network to be robust to detection errors, we follow the dynamic zoom-in setting suggested in [24] where noisy ground truth bounding boxes are used in the training phase, and detected bounding box from detectors such as [36] and [35] are used in the test phase. Note that the bounding box from dynamic zoom-in is also used in our grid cropping process included in the DProST.

4.3. Comparison with State-of-the-Art

Table 1 presents the results of our method on the LM dataset. As shown in the table, our method shows state-of-the-art accuracy on the LINEMOD dataset without CAD data. Compared to a render-and-compare-based method ([23]), which uses CAD data and PM loss, our method shows more accurate results in almost every object. Also, compared to [29], which also does not need a CAD model for an object of interest but requires the depth map, our method shows superior performance without using any depth data. The qualitative results are visualized in Figure 4. Also, the accuracy of the LMO dataset is described in Table 2. Our method shows comparable results on the LMO dataset but does not outperform the methods that fully exploit the CAD information.

4.4. Ablation Studies

We conduct ablation studies to check the effectiveness of iteration, BiZ-buffer, and PGDL, and the results are shown in Table 3. First, we test our method with the number of iterations. The result shows that the performance is clearly improved in the second iteration, but saturated in more iterations. Second, we validate the benefit of PGDL com-

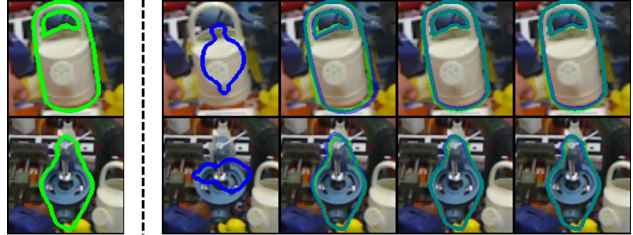


Figure 5. **Iterative Pose Estimation Results.** Illustration of ground-truth pose in green contours and initial pose and predicted poses in blue contours. Each image from second column to fifth column indicates the initial pose and the result from each iteration.

pared to Point Matching(PM) loss used in [21,23,45]. Since PM requires a CAD model to calculate the distance between vertices, we use the object CAD for this setting. Thanks to the overall advantages in section 3.3.3, PGDL shows better performance than PM even without using any CAD information. We also conduct the evaluation of BiZ-buffering on the LM dataset. Without BiZ-buffer, our network only takes the front view of the object from Equation (11). As shown in Table 3, using the BiZ-buffer shows slightly better performance but does not improve the accuracy significantly. More details about ablation studies are given in the supplementary material.

5. Conclusion

We have proposed a new 6D object pose estimation method that does not require CAD data. For this, we have designed a space-carving-based reconstruction module and a DProST-based projection module. Our proposed DProST elaborately considers the perspective distortion while reducing the number of parameters and computation by the dynamic grid pushing method. Based on the aligned grid from DProST, we suggest a method to extract both the front view and self-occluded back view of the object, named BiZ-buffering. Also, we introduced a new loss function, PGDL, which considers the perspective distortion of images and can be used to train the model without CAD data. Experiments show that our method outperforms the state-of-the-art pose estimation method even without CAD data in the benchmark dataset. We plan to apply the DProST method to other 3D reconstruction methods based on deep learning in the future. Also, applying our method to unseen or categorical objects would be one way for future research.

References

- [1] Mark Boss, Raphael Braun, Varun Jampani, Jonathan T Barron, Ce Liu, and Hendrik Lensch. Nerd: Neural reflectance decomposition from image collections. In *Proceedings of the IEEE/CVF International Conference on Computer Vision*, pages 12684–12694, 2021. 3

- [2] Eric Brachmann, Alexander Krull, Frank Michel, Stefan Gumhold, Jamie Shotton, and Carsten Rother. Learning 6d object pose estimation using 3d object coordinates. In *European conference on computer vision*, pages 536–551. Springer, 2014. [6](#)
- [3] Eric Brachmann, Frank Michel, Alexander Krull, Michael Ying Yang, Stefan Gumhold, et al. Uncertainty-driven 6d pose estimation of objects and scenes from a single rgb image. In *Proceedings of the IEEE conference on computer vision and pattern recognition*, pages 3364–3372, 2016. [1](#), [6](#)
- [4] Zhaowei Cai and Nuno Vasconcelos. Cascade r-cnn: Diving into high quality object detection. In *Proceedings of the IEEE conference on computer vision and pattern recognition*, pages 6154–6162, 2018. [7](#)
- [5] Xiaozhi Chen, Huimin Ma, Ji Wan, Bo Li, and Tian Xia. Multi-view 3d object detection network for autonomous driving. In *Proceedings of the IEEE conference on Computer Vision and Pattern Recognition*, pages 1907–1915, 2017. [1](#)
- [6] Yi Cheng, Hongyuan Zhu, Ying Sun, Cihan Acar, Wei Jing, Yan Wu, Liyuan Li, Cheston Tan, and Joo-Hwee Lim. 6d pose estimation with correlation fusion. In *2020 25th International Conference on Pattern Recognition (ICPR)*, pages 2988–2994. IEEE, 2021. [1](#)
- [7] Christopher B Choy, Danfei Xu, JunYoung Gwak, Kevin Chen, and Silvio Savarese. 3d-r2n2: A unified approach for single and multi-view 3d object reconstruction. In *European conference on computer vision*, pages 628–644. Springer, 2016. [3](#)
- [8] Jia Deng, Wei Dong, Richard Socher, Li-Jia Li, Kai Li, and Li Fei-Fei. Imagenet: A large-scale hierarchical image database. In *2009 IEEE conference on computer vision and pattern recognition*, pages 248–255. Ieee, 2009. [7](#)
- [9] Yan Di, Fabian Manhardt, Gu Wang, Xiangyang Ji, Nassir Navab, and Federico Tombari. So-pose: Exploiting self-occlusion for direct 6d pose estimation. In *Proceedings of the IEEE/CVF International Conference on Computer Vision*, pages 12396–12405, 2021. [1](#), [2](#), [7](#)
- [10] Cong Gao, Xingtong Liu, Wenhao Gu, Benjamin Killeen, Mehran Armand, Russell Taylor, and Mathias Unberath. Generalizing spatial transformers to projective geometry with applications to 2d/3d registration. In *International Conference on Medical Image Computing and Computer-Assisted Intervention*, pages 329–339. Springer, 2020. [2](#), [3](#), [5](#), [11](#)
- [11] Georgia Gkioxari, Jitendra Malik, and Justin Johnson. Mesh r-cnn. In *Proceedings of the IEEE/CVF International Conference on Computer Vision*, pages 9785–9795, 2019. [3](#)
- [12] Kaifeng He, Xiangyu Zhang, Shaoqing Ren, and Jian Sun. Deep residual learning for image recognition. In *Proceedings of the IEEE conference on computer vision and pattern recognition*, pages 770–778, 2016. [7](#)
- [13] Stefan Hinterstoisser, Vincent Lepetit, Slobodan Ilic, Stefan Holzer, Gary Bradski, Kurt Konolige, and Nassir Navab. Model based training, detection and pose estimation of texture-less 3d objects in heavily cluttered scenes. In *Asian conference on computer vision*, pages 548–562. Springer, 2012. [6](#), [7](#)
- [14] Tomáš Hodaň, Martin Sundermeyer, Bertram Drost, Yann Labbé, Eric Brachmann, Frank Michel, Carsten Rother, and Jiří Matas. Bop challenge 2020 on 6d object localization. In *European Conference on Computer Vision*, pages 577–594. Springer, 2020. [2](#), [6](#)
- [15] Yinlin Hu, Pascal Fua, Wei Wang, and Mathieu Salzmann. Single-stage 6d object pose estimation. In *Proceedings of the IEEE/CVF conference on computer vision and pattern recognition*, pages 2930–2939, 2020. [1](#)
- [16] Yinlin Hu, Joachim Hugonot, Pascal Fua, and Mathieu Salzmann. Segmentation-driven 6d object pose estimation. In *Proceedings of the IEEE/CVF Conference on Computer Vision and Pattern Recognition*, pages 3385–3394, 2019. [1](#), [2](#)
- [17] Shun Iwase, Xingyu Liu, Rawal Khirodkar, Rio Yokota, and Kris M Kitani. Repose: Real-time iterative rendering and refinement for 6d object pose estimation. *arXiv preprint arXiv:2104.00633*, 2021. [2](#), [7](#)
- [18] Max Jaderberg, Karen Simonyan, Andrew Zisserman, et al. Spatial transformer networks. *Advances in neural information processing systems*, 28:2017–2025, 2015. [4](#), [5](#)
- [19] Diederik P Kingma and Jimmy Ba. Adam: A method for stochastic optimization. *arXiv preprint arXiv:1412.6980*, 2014. [7](#)
- [20] Kiriakos N Kutulakos and Steven M Seitz. A theory of shape by space carving. *International journal of computer vision*, 38(3):199–218, 2000. [2](#), [3](#)
- [21] Yann Labbé, Justin Carpentier, Mathieu Aubry, and Josef Sivic. Cosypose: Consistent multi-view multi-object 6d pose estimation. In *European Conference on Computer Vision*, pages 574–591. Springer, 2020. [1](#), [2](#), [3](#), [6](#), [7](#), [8](#)
- [22] Vincent Lepetit, Francesc Moreno-Noguer, and Pascal Fua. Epnnp: An accurate o(n) solution to the pnp problem. *International journal of computer vision*, 81(2):155, 2009. [2](#)
- [23] Yi Li, Gu Wang, Xiangyang Ji, Yu Xiang, and Dieter Fox. Deepim: Deep iterative matching for 6d pose estimation. In *Proceedings of the European Conference on Computer Vision (ECCV)*, pages 683–698, 2018. [1](#), [2](#), [3](#), [6](#), [7](#), [8](#), [11](#), [12](#)
- [24] Zhigang Li, Gu Wang, and Xiangyang Ji. Cdpn: Coordinates-based disentangled pose network for real-time rgb-based 6-dof object pose estimation. In *Proceedings of the IEEE/CVF International Conference on Computer Vision*, pages 7678–7687, 2019. [1](#), [2](#), [7](#), [8](#)
- [25] Eric Marchand, Hideaki Uchiyama, and Fabien Spindler. Pose estimation for augmented reality: a hands-on survey. *IEEE transactions on visualization and computer graphics*, 22(12):2633–2651, 2015. [1](#)
- [26] Ben Mildenhall, Pratul P Srinivasan, Matthew Tancik, Jonathan T Barron, Ravi Ramamoorthi, and Ren Ng. Nerf: Representing scenes as neural radiance fields for view synthesis. In *European conference on computer vision*, pages 405–421. Springer, 2020. [3](#)
- [27] Thu Nguyen-Phuoc, Chuan Li, Stephen Balaban, and Yong-Liang Yang. Rendernet: A deep convolutional network for differentiable rendering from 3d shapes. In *Advances in Neural Information Processing Systems 31*, 2018. [3](#)
- [28] Markus Oberweger, Mahdi Rad, and Vincent Lepetit. Making deep heatmaps robust to partial occlusions for 3d object

- pose estimation. In *Proceedings of the European Conference on Computer Vision (ECCV)*, pages 119–134, 2018. 1
- [29] Keunhong Park, Arsalan Mousavian, Yu Xiang, and Dieter Fox. Latentfusion: End-to-end differentiable reconstruction and rendering for unseen object pose estimation. In *Proceedings of the IEEE/CVF conference on computer vision and pattern recognition*, pages 10710–10719, 2020. 2, 3, 7, 8
- [30] Kiru Park, Timothy Patten, and Markus Vincze. Pix2pose: Pixel-wise coordinate regression of objects for 6d pose estimation. In *Proceedings of the IEEE/CVF International Conference on Computer Vision*, pages 7668–7677, 2019. 1, 2
- [31] Adam Paszke, Sam Gross, Francisco Massa, Adam Lerer, James Bradbury, Gregory Chanan, Trevor Killeen, Zeming Lin, Natalia Gimelshein, Luca Antiga, et al. Pytorch: An imperative style, high-performance deep learning library. *Advances in neural information processing systems*, 32:8026–8037, 2019. 7
- [32] Sida Peng, Yuan Liu, Qixing Huang, Xiaowei Zhou, and Hujun Bao. Pvnnet: Pixel-wise voting network for 6dof pose estimation. In *Proceedings of the IEEE/CVF Conference on Computer Vision and Pattern Recognition*, pages 4561–4570, 2019. 1, 2
- [33] Mahdi Rad and Vincent Lepetit. Bb8: A scalable, accurate, robust to partial occlusion method for predicting the 3d poses of challenging objects without using depth. In *Proceedings of the IEEE International Conference on Computer Vision*, pages 3828–3836, 2017. 1, 2
- [34] Nikhila Ravi, Jeremy Reizenstein, David Novotny, Taylor Gordon, Wan-Yen Lo, Justin Johnson, and Georgia Gkioxari. Accelerating 3d deep learning with pytorch3d. *arXiv preprint arXiv:2007.08501*, 2020. 7
- [35] Joseph Redmon and Ali Farhadi. Yolov3: An incremental improvement. *arXiv preprint arXiv:1804.02767*, 2018. 8
- [36] Shaoqing Ren, Kaiming He, Ross Girshick, and Jian Sun. Faster r-cnn: Towards real-time object detection with region proposal networks. *Advances in neural information processing systems*, 28:91–99, 2015. 3, 8
- [37] Vincent Sitzmann, Justus Thies, Felix Heide, Matthias Nießner, Gordon Wetzstein, and Michael Zollhofer. Deepvoxels: Learning persistent 3d feature embeddings. In *Proceedings of the IEEE/CVF Conference on Computer Vision and Pattern Recognition*, pages 2437–2446, 2019. 2, 3
- [38] Chen Song, Jiaru Song, and Qixing Huang. Hybridpose: 6d object pose estimation under hybrid representations. In *Proceedings of the IEEE/CVF conference on computer vision and pattern recognition*, pages 431–440, 2020. 1, 2, 7
- [39] Bugra Tekin, Sudipta N Sinha, and Pascal Fua. Real-time seamless single shot 6d object pose prediction. In *Proceedings of the IEEE Conference on Computer Vision and Pattern Recognition*, pages 292–301, 2018. 1
- [40] Jonathan Tremblay, Thang To, Balakumar Sundaralingam, Yu Xiang, Dieter Fox, and Stan Birchfield. Deep object pose estimation for semantic robotic grasping of household objects. In *Conference on Robot Learning*, pages 306–316. PMLR, 2018. 1
- [41] Chen Wang, Danfei Xu, Yuke Zhu, Roberto Martín-Martín, Cewu Lu, Li Fei-Fei, and Silvio Savarese. Densefusion: 6d object pose estimation by iterative dense fusion. In *Proceedings of the IEEE/CVF conference on computer vision and pattern recognition*, pages 3343–3352, 2019. 1
- [42] Gu Wang, Fabian Manhardt, Federico Tombari, and Xiangyang Ji. Gdr-net: Geometry-guided direct regression network for monocular 6d object pose estimation. In *Proceedings of the IEEE/CVF Conference on Computer Vision and Pattern Recognition*, pages 16611–16621, 2021. 1, 2, 7
- [43] He Wang, Srinath Sridhar, Jingwei Huang, Julien Valentin, Shuran Song, and Leonidas J Guibas. Normalized object coordinate space for category-level 6d object pose and size estimation. In *Proceedings of the IEEE/CVF Conference on Computer Vision and Pattern Recognition*, pages 2642–2651, 2019. 1, 2
- [44] Nanyang Wang, Yinda Zhang, Zhuwen Li, Yanwei Fu, Wei Liu, and Yu-Gang Jiang. Pixel2mesh: Generating 3d mesh models from single rgb images. In *Proceedings of the European Conference on Computer Vision (ECCV)*, pages 52–67, 2018. 3
- [45] Yu Xiang, Tanner Schmidt, Venkatraman Narayanan, and Dieter Fox. Posecnn: A convolutional neural network for 6d object pose estimation in cluttered scenes. In *Proceedings of Robotics: Science and Systems*, Pittsburgh, Pennsylvania, June 2018. 1, 6, 7, 8
- [46] Danfei Xu, Dragomir Anguelov, and Ashesh Jain. Pointfusion: Deep sensor fusion for 3d bounding box estimation. In *Proceedings of the IEEE conference on computer vision and pattern recognition*, pages 244–253, 2018. 1
- [47] Zongxin Yang, Xin Yu, and Yi Yang. Dsc-posenet: Learning 6dof object pose estimation via dual-scale consistency. In *Proceedings of the IEEE/CVF Conference on Computer Vision and Pattern Recognition*, pages 3907–3916, 2021. 2
- [48] Sergey Zakharov, Ivan Shugurov, and Slobodan Ilic. Dpod: 6d pose object detector and refiner. In *Proceedings of the IEEE/CVF International Conference on Computer Vision*, pages 1941–1950, 2019. 2, 7
- [49] Yi Zhou, Connelly Barnes, Jingwan Lu, Jimei Yang, and Hao Li. On the continuity of rotation representations in neural networks. In *Proceedings of the IEEE/CVF Conference on Computer Vision and Pattern Recognition*, pages 5745–5753, 2019. 7
- [50] Menglong Zhu, Konstantinos G Derpanis, Yinfei Yang, Samarth Brahmabhatt, Mabel Zhang, Cody Phillips, Matthieu Lecce, and Kostas Daniilidis. Single image 3d object detection and pose estimation for grasping. In *2014 IEEE International Conference on Robotics and Automation (ICRA)*, pages 3936–3943. IEEE, 2014. 1

A. Details of Grid Sampling in DProST.

In DProST, we use the same 3D grid sampling used in [10]. Specifically, to extract values from the 3D feature, we use trilinear interpolation-based grid sampling. For each iteration t , the 3D feature $(\hat{\mathcal{F}}_t^T \in \mathbb{R}^{\hat{h}^B \times \hat{w}^B \times N_z})$ is interpolated from the 3D reference $(\mathcal{F}^{ref} \in \mathbb{R}^{S \times S \times S \times 3})$ at the grid points $(\hat{\mathcal{G}}_t^T \in \mathbb{R}^{\hat{h}^B \times \hat{w}^B \times N_z})$, where \hat{h}^B and \hat{w}^B are height and width of bounding box respectively, N_z is the number of vertices along the ray, and S^3 is the number of the voxels in the 3D reference. The above interpolation can be written as

$$\begin{aligned} \hat{\mathcal{F}}_t^T(i, j, k) &= \sum_n^S \sum_m^S \sum_l^S \mathcal{F}^{ref}(n, m, l) \\ &\max(0, 1 - |(\hat{g}_t^T)_x - n|) \max(0, 1 - |(\hat{g}_t^T)_y - m|) \\ &\max(0, 1 - |(\hat{g}_t^T)_z - l|) \end{aligned} \quad (16)$$

where $(\hat{g}_t^T)_x$, $(\hat{g}_t^T)_y$, and $(\hat{g}_t^T)_z$ are (x, y, z) coordinates in $\hat{\mathcal{G}}_t^T(i, j, k)$.

B. Derivation of PGDL

The PGDL can be written with cropped grid and coefficient, $(\hat{\mathcal{G}}^B, \hat{\mathcal{C}}^B)$, as follows:

$$\begin{aligned} \mathcal{L}_t^{PGDL}(\bar{T}, \hat{T}_t) &= \frac{1}{|\hat{\mathcal{G}}^B|} \sum_{(i,j,k) \in S^{\mathcal{G}}} \left\| \bar{\mathcal{G}}^T(i, j, k) - \hat{\mathcal{G}}_t^T(i, j, k) \right\|_2 \quad (17) \\ &= \frac{1}{|\hat{\mathcal{G}}^B|} \sum_{(i,j,k) \in S^{\mathcal{G}}} \left\| \bar{T}(\bar{\mathcal{G}}^P(i, j, k)) - \hat{T}_t(\hat{\mathcal{G}}_t^P(i, j, k)) \right\|_2 \\ &= \frac{1}{|\hat{\mathcal{G}}^B|} \sum_{(i,j,k) \in S^{\mathcal{G}}} \left\| \bar{T}(\hat{\mathcal{G}}^B(i, j, k) + \|\bar{\mathbf{t}}\|_2 \hat{\mathcal{C}}^B(i, j, k)) \right. \\ &\quad \left. - \hat{T}_t(\hat{\mathcal{G}}^B(i, j, k) + \|\hat{\mathbf{t}}_t\|_2 \hat{\mathcal{C}}^B(i, j, k)) \right\|_2 \quad (18) \end{aligned}$$

where $S^{\mathcal{G}} = \{(i, j, k) | 1 \leq i \leq \hat{h}^B, 1 \leq j \leq \hat{w}^B, 1 \leq k \leq N_z\}$, \bar{T} and \hat{T}_t are ground truth pose and the t -th step predicted pose, $\bar{\mathcal{G}}^P$ and $\hat{\mathcal{G}}_t^P$ are pushed-grid based on ground truth translation $(\bar{\mathbf{t}})$ and predicted translation $(\hat{\mathbf{t}}_t)$, respectively. Since both $\bar{\mathcal{G}}^T$ and $\hat{\mathcal{G}}_t^T$ are computed based on $\hat{\mathcal{G}}^B$ and $\hat{\mathcal{C}}^B$, the PGDL is proportional only to the pose difference. In other words, $\hat{\mathcal{G}}^B$ and $\hat{\mathcal{C}}^B$ work as a constant, and the optimization target of the PGDL is the difference between the \bar{T} and the \hat{T}_t .

C. Additional Ablation Study

We show the detailed evaluation of LM in Table C.1. In order to compare how accurately our method predicts the

pose, we measure the ADD(-S) score with thresholds of 0.02, 0.05, and 0.10 diameter of the object, respectively. Also, we test the 2D projection error, which focuses on the matching of pose estimation on 2D images, with thresholds of 2, 5, and 10 pixels to check whether the appearance of the object is matched with the label pose. Compared to DeepIM [23], which is the previous render-and-compare method, our method outperforms overall in various settings.

D. Additional Qualitative Results

We demonstrate the example result of each iteration step in Figure D.1. In order to visualize the results of the BiZ-buffer, we illustrate the front view and back view from the BiZ-buffer of objects in LMO in Figure D.2. Also, Figure D.3 visualizes the deterioration that occurs when N and N_z are smaller than the default values of 8 and 100. Lastly, we illustrate additional qualitative results of LMO in Figure D.4.

Method	Iteration	BiZ-buffer	Loss	N_z	N	ADD(-S)			Proj.2D		
						0.02d	0.05d	0.10d	2pix	5pix	10pix
DeepIM [23]						30.9	69.2	88.6	75.6	97.5	99.7
Ours	1	✓	PGDL	100	8	17.7	60.5	86.9	55.3	95.5	99.9
Ours	2	✓	PGDL	100	8	43.3	83.6	96.5	87.0	98.3	99.3
Ours	3		PGDL	100	8	44.6	83.6	96.7	86.8	98.6	99.9
Ours	3	✓	PM	100	8	37.7	77.1	93.5	79.0	97.9	99.7
Ours	3	✓	PGDL	50	8	41.3	80.0	93.7	84.2	95.9	97.5
Ours	3	✓	PGDL	100	2	36.7	77.7	94.1	81.9	98.5	99.8
Ours	3	✓	PGDL	100	4	39.9	80.4	95.3	83.8	97.2	98.8
Ours	3	✓	PGDL	100	8	43.5	83.4	96.8	86.8	98.2	99.3

Table C.1. **Details of Ablation Study on LM.** We compare the effectiveness of the number of iterations, BiZ-buffer, and PGDL on LM in detail. We also compare the results according to the number of grid along rays (N_z), and the number of reference images (N).

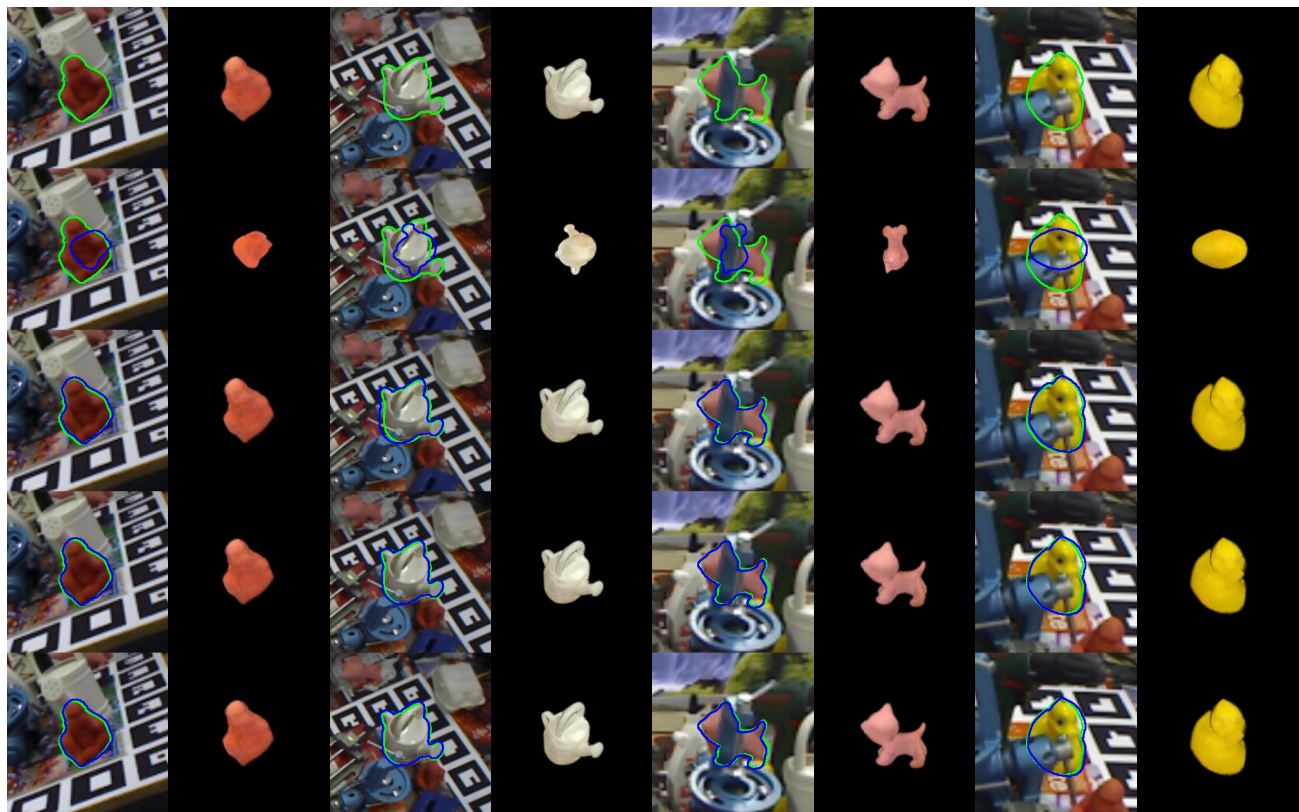


Figure D.1. **Iterative Results on LMO.** Some examples of pose refinement results on the LMO dataset. Each odd numbered column shows the contour of the label pose in green and the prediction in blue. Each even numbered column demonstrates the DProST and BiZ-buffered front view of the corresponding pose. The first row shows the label pose of each object and the second to the fifth show the initial pose and refinement of each iteration in order.

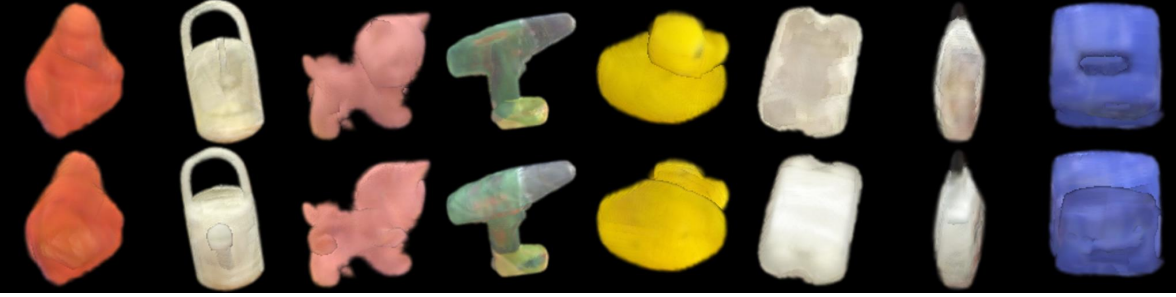


Figure D.2. **Examples of Front View and Back View Results of BiZ-buffer on Objects in LMO.** The first row shows the front view (\hat{F}_t^f) and the second illustrates the back view (\hat{F}_t^b) from BiZ-buffer method. Note that since the DProST aligns the grid along the ray, the outlines of the two views are same.



Figure D.3. **Visualization of BiZ-buffer Results According to N and N_z on Objects in LMO.** The first row shows the examples of front view (\hat{F}_t^f) from BiZ-buffer on default setting ($N_z = 100, N = 8$). The second row visualize the examples of \hat{F}_t^f when N_z is reduced to half ($N_z = 50, N = 8$). Each third and fourth row illustrates the examples of \hat{F}_t^f when N is reduced to half ($N_z = 100, N = 4$) and quarter ($N_z = 100, N = 2$).

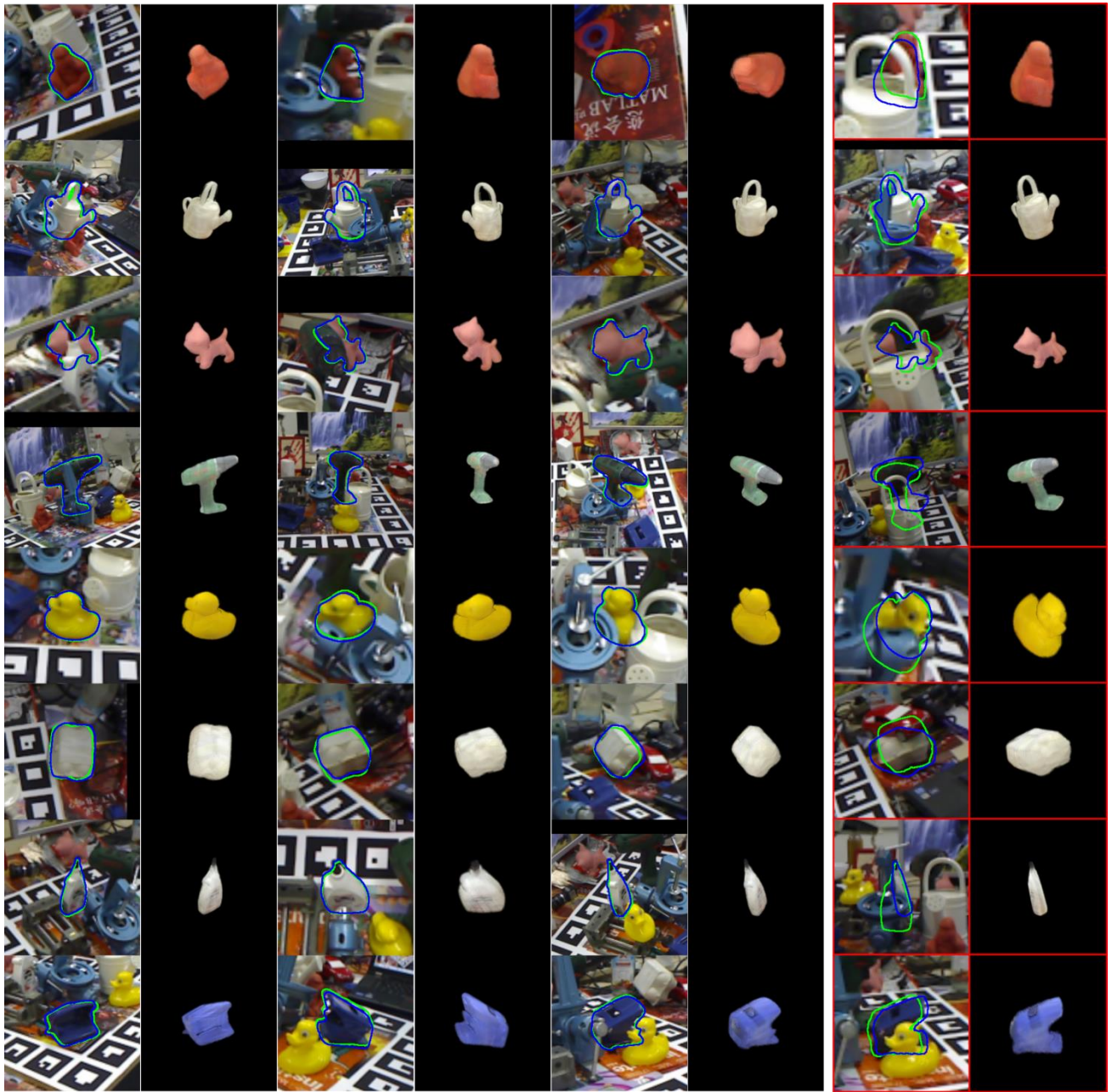


Figure D.4. **Qualitative Results on LMO.** We demonstrate the qualitative results on the LMO dataset. Each odd number column shows the contour of the label pose in green and the prediction in blue, and each even number column illustrates the DProST and BiZ-buffered front view of the estimated pose. Also, the rightmost two boxes (marked with red boxes) are the cases that errors occurred due to excessive occlusion.